Journal of Power Sources 195 (2010) 621–630

Contents lists available at ScienceDirect

Journal of Power Sources

journal homepage: www.elsevier.com/locate/jpowsour

The interrelation between mechanical properties, corrosion resistance and microstructure of Pb–Sn casting alloys for lead-acid battery components

Leandro C. Peixoto, Wislei R. Osório*, Amauri Garcia

Department of Materials Engineering, University of Campinas – UNICAMP, PO Box 6122, 13083-970, Campinas - SP, Brazil

ARTICLE INFO

Article history:
Received 25 June 2009
Accepted 8 August 2009
Available online 15 August 2009

Keywords:
Lead-acid battery
Cellular microstructure
Ultimate tensile strength
Electrochemical impedance
Corrosion resistance

ABSTRACT

It is well known that there is a strong influence of thermal processing variables on the solidification structure and as a direct consequence on the casting final properties. The morphological microstructural parameters such as grain size and cellular or dendritic spacings will depend on the heat transfer conditions imposed by the metal/mould system. There is a need to improve the understanding of the interrelation between the microstructure, mechanical properties and corrosion resistance of dilute Pb–Sn casting alloys which are widely used in the manufacture of battery components. The present study has established correlations between cellular microstructure, ultimate tensile strength and corrosion resistance of Pb–1 wt% Sn and Pb–2.5 wt% Sn alloys by providing a combined plot of these properties as a function of cell spacing. It was found that a compromise between good corrosion resistance and good mechanical properties can be attained by choosing an appropriate cell spacing range.

1. Introduction

A battery grid must be dimensionally stable and have mechanical properties which can resist the stresses of the charge/discharge reactions without bending, stretching or warping. Pb–Sn, Pb–Sb and Pb–Ca–Sn alloys are commonly used in the production of positive and negative grids, connectors, posts and straps components of both VRLA and SLI batteries which are widely applied in automotive and telecommunication services [1–3]. It is reported that Pb–Sn (Ca) and Pb–Sn alloys can be better alternatives for the production of Pb-acid battery grids with a view to achieving a maintenance-free condition [4–11]. Considering the strength of grids, it is known that they are highly dependent on alloying content. In this context, the effects of alloying additions have been studied for a whole range of alloys compositions [4–17].

The effect of microstructure on metallic alloys properties has been highlighted in various studies and particularly, the influence of dendrite arm spacing upon the mechanical properties, i.e., ultimate tensile strength and yield strength, has been reported [18–26]. Recently, some studies have also focused on dendritic or cellular networks and corrosion behavior relationships [26–32]. Although the metallurgical and micromechanical aspects of the factors controlling microstructure, unsoundness, strength and ductility, and corrosion resistance of as-cast alloys are complex, it is well known that solidification processing variables play an extremely important role. In the as-cast state, an alloy may possess within individual grains a dendritic network of continuously varying solute content, second phases and possibly porosity and inclusions [21]. It is generally found that the grain size reduction increases the metal tensile strength. The well known Hall–Petch equation shows that the yield strength is proportional to the reciprocal of the square root of the grain diameter [18,19]. For cast metals, however, it is not always true that the tensile strength improves with decreasing grain size. Strength will increase with grain size reduction only if the production of small grains does not increase the amount of microporosity, the volume fraction of second phase or the dendrite spacing [23]. It is not also always true that finer microstructures provide improvement in the corrosion resistance.

The cooling rate during solidification defines the scale of cellular and dendritic microstructural networks. Thus, the control of solidification thermal variables such as tip growth rate (V_L) and cooling rate ($\dot{T}$) can permit a wide range of microstructures to be obtained. The solute redistribution, the anodic or cathodic electrochemical behavior of each component of the alloy and the microstructure fineness are the three main factors affecting the corrosion resistance of castings [26–28]. Razaei and Damiri [7] have reported that the control of solidification variables has an important role on the electrochemical behavior of lead-acid battery grid alloys. It was also reported that coarse cellular microstructures of Pb–Sn and Pb–Sb alloys are associated with better electrochemical corrosion resistance than fine microstructures [30–34]. However, the literature is scarce on reports interrelating solidification parameters, castings microstructure and optimized mechanical and corrosion properties.

* Corresponding author. Tel.: +55 19 3521 3320; fax: +55 19 3289 3722.
E-mail address: wislei@fem.unicamp.br (W.R. Osório).

0378-7753/$ – see front matter © 2009 Elsevier B.V. All rights reserved.
doi:10.1016/j.jpowsour.2009.08.011

There is a need to improve the understanding of the interrelation between the microstructure, mechanical properties and corrosion resistance of dilute Pb–Sn casting alloys which are widely used in the manufacture of battery components. In this context, the present investigation aims to contribute to provide a basis for understanding how to control solidification parameters and casting microstructure, in order to achieve a compromise between the resistance to corrosion action and the mechanical strength of Pb–1 wt% Sn and Pb–2.5 wt% Sn alloys. Experimental results include transient metal/mould heat transfer coefficient and cooling rate during solidification, cellular array parameters, corrosion potential, corrosion rate, polarization resistances, capacitance values, ultimate tensile strength, yield strength and elongation.

2. Solidification thermal variables

Heat flow across the casting/mold interface can be characterized by a macroscopic average metal/mold interfacial heat transfer coefficient, h_i [W m^{-2} K^{-1}], given by:

$$h_i = \frac{q}{A(T_{IC} - T_{IM})} \quad (1)$$

where q [W] is the average heat flux, A [m^2] is the area and T_{IC} and T_{IM} are metal and mold surface temperatures [K] at the interface. It is well known that during the solidification process, the mold gradually expands due to heat absorption, and the metal casting is subjected to shrinkage. As a result, a gap develops due to insufficient contact between metal and mold, and as a direct consequence, h_i decreases rapidly. In previous articles the transient interfacial heat transfer coefficient has been successfully characterized by using an approach based on measured temperatures along the casting and numerical simulations provided by heat transfer solidification models [26–29,35–37]. This coefficient has been expressed as a power function of time:

$$h_i = C_i(t)^{-a} \quad (2)$$

where t [s] is the time from the beginning of cooling during the solidification process and C_i and a are the constants which depend on alloy composition, mold material and melt superheat.

Solidification thermal variables can be described as a function of metal/mold parameters and casting operational conditions and consequently, as a function of the metal/mold interfacial heat transfer coefficient (h_i) [26–29,35–37]. An analytical heat transfer model describing temperature distribution in liquid, mushy zone, solid, mold and the displacement of solidus and liquidus isotherms during the unidirectional solidification of binary alloys, can be used for determining the cell tip cooling rate during solidification ($\dot{T}$), and is given by [37]:

$$\dot{T} = \frac{4m\phi_2(T_p - T_L)\,\alpha_L}{\sqrt{\pi}\,[1 - erf(m\phi_2)]\exp(m\phi_2)^2} V_L^2 \quad (3)$$

and V_L, which is the tip growth rate is given by (4):

$$V_L = \frac{2\alpha_{SL}{\phi_2}^2}{\{[2K_S\phi_2(T_S - T_0)]/[n\sqrt{\pi}(T_L - T_0)\exp{\phi_1}^2(M + erf\,\phi_1)h_i]\} + S_L} \quad (4)$$

where K is the thermal conductivity, c is the specific heat, ρ is the density (subscripts S, SL and L represent solid, mushy and liquid phases, respectively), m is the square root of ratio of thermal diffusivities of mushy zone and liquid $(\alpha_{SL}/\alpha_L)^{1/2}$, α is the liquid thermal diffusivity $(Kc^{-1}\rho^{-1})$, T_p is the pouring temperature, ϕ_1 and ϕ_2 are solidification constants associated with the displacement of the solidus and liquidus isotherms, respectively, T_S is the non-equilibrium solidus temperature, T_0 is the environment temperature, T_L is the liquidus temperature, M is the ratio of heat diffusivities of solid and mold material, $[(k_Sc_S\rho_S)/(k_Mc_M\rho_M)]^{1/2}$, n is the square root of the ratio of thermal diffusivities of solid metal and mushy zone $(\alpha_S/\alpha_{SL})^{1/2}$, S_L is the position of liquidus isotherm from the metal/mold interface. It can be seen from Eqs. (3) and (4), that important thermal variables associated with the casting process, such as tip cooling rate and tip growth rate are related to h_i, as well as to metal/mold casting parameters.

3. Experimental procedure

3.1. Specimen preparation

Pb–1 wt% Sn and Pb–2.5 wt% Sn alloys were prepared by using commercially pure metals: Pb (99.89 wt%) and Sn (99.99 wt%). The mean impurities were: Fe (0.12%), Si (0.05%), Cu (0.015%), besides other elements with concentration less than 50 ppm.

A water-cooled unidirectional solidification system was used in the experiments. The solidification set-up was designed in such way that the heat was extracted only through the water-cooled bottom, promoting vertical upward directional solidification. The temperatures were monitored during solidification using a bank of type J thermocouples accurately located along the casting length at six different positions with respect to the metal/mold interface: 4; 12; 22; 38; 54 and 68 mm, at the centre of the casting, as detailed in previous articles [30–34]. All the thermocouples were connected by coaxial cables to a data logger interfaced with a computer, and the temperature data were acquired automatically. The thermophysical properties of the dilute Pb–Sn alloys, which

Table 1
Thermophysical properties of Pb–Sn used for simulations.

Properties	Symbols [units]	Pb	Pb–1.0% Sn	Pb–2.5% Sn	Sn
Liquidus temperature	T_L [°C]	–	326	321	–
Melting temperature	T_f [°C]	327.5	–	–	231.97
Thermal conductivity					
Solid	k_S [W m^{-1} K^{-1}]	34.7	34.9	35.1	67
Liquid	k_L [W m^{-1} K^{-1}]	29.7	29.7	29.7	33
Specific heat					
Solid	c_S [J kg^{-1} K^{-1}]	129.8	130.3	131.1	267
Liquid	c_L [J kg^{-1} K^{-1}]	138.2	138.9	139.9	257
Density					
Solid	ρ_S [kg m^{-3}]	11,340	11,316	11,284	7,166
Liquid	ρ_L [kg m^{-3}]	10,678	10,654	10,627	6,986
Latent heat of fusion	L [J kg^{-1}]	26,205	26,406	26,680	60,700
Partition coefficient	k_o		0.296	0.296	

were used to run the necessary simulations, are summarized in Table 1.

As-cast specimens were sectioned from the center of the casting, ground, polished and etched to reveal the macrostructure (the etchant was a mixture of aqueous solutions: 3:1 – in volume – HNO_3 solution and 6:1 – in volume – ammonium molybdate). The samples were polished and etched by using a 37 cm^3 glacial acetic acid and 15 cm^3 of hydrogen peroxide solution at room temperature for microscopy examination. The microstructural characterization was carried out by using an optical microscope associated with an image processing system Neophot 32 (Carl Zeiss, Esslingen, Germany) and Leica Quantimet 500 MC (Leica Imaging Systems Ltd., Cambridge, England).

3.2. Tensile testing

Fig. 1(a) and (b) depicts the typical macrostructure of the Pb–1 wt% Sn and Pb–2.5 wt% Sn alloys castings which were obtained in directional solidification experiments. It can be seen that the growth of columnar grains prevailed along the entire casting length. Fig. 1(c) shows a schematic representation of the specimens for the tensile tests and the position from where they were extracted along the casting length. These specimens were prepared according to the specifications of ASTM Standard E 8M/04 and tested in a MTS Test Star II machine at a strain rate of $1 \times 10^{-3}\ s^{-1}$ in the elastic range and of $4 \times 10^{-3}\ s^{-1}$ in the plastic range. In order to ensure reproducibility of the tensile results, three specimens were tested

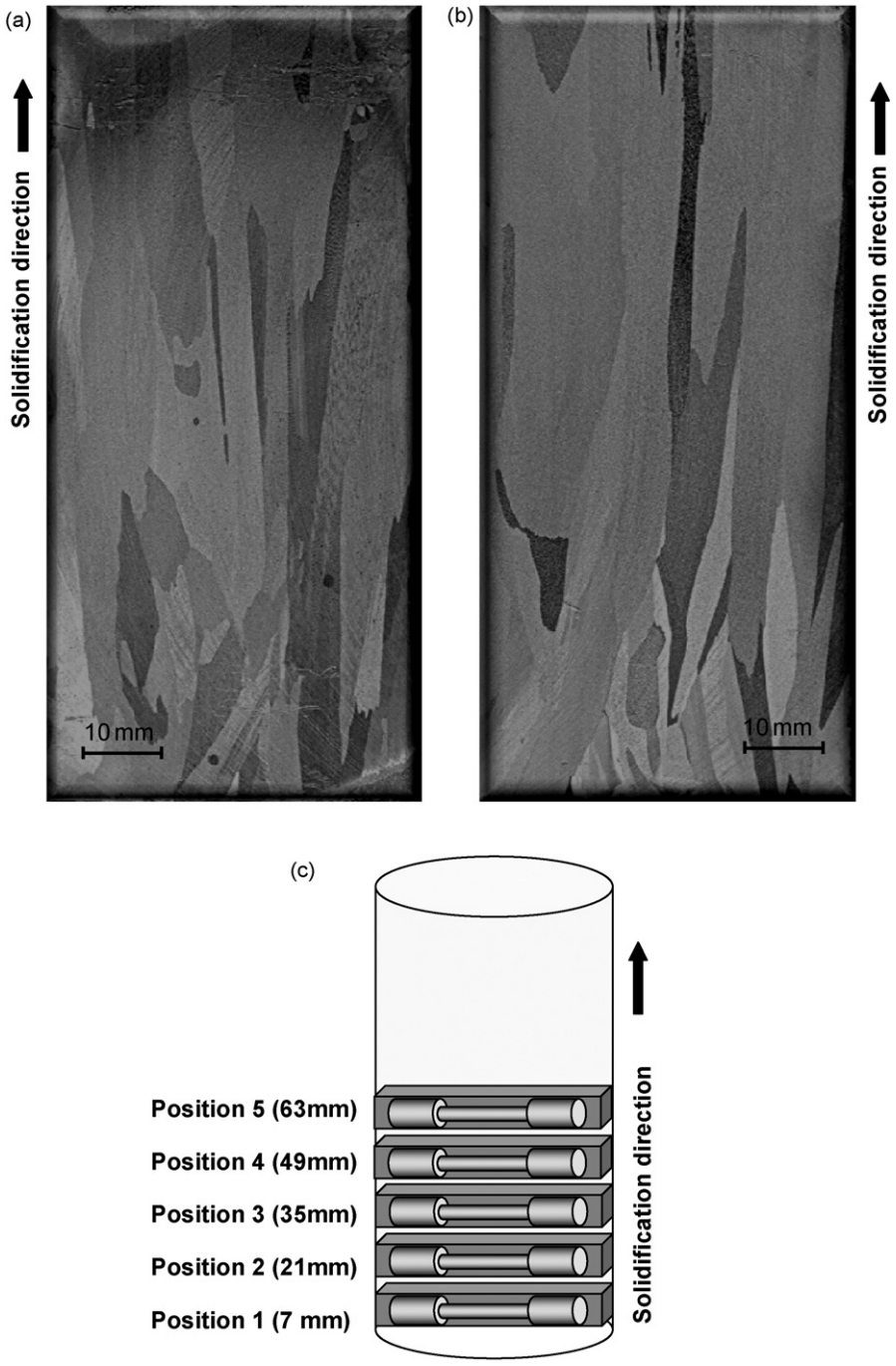

Fig. 1. Macrostructures of upward directionally solidified castings: (a) Pb–1 wt% Sn and (b) Pb–2.5 wt% Sn alloys evidencing the columnar growth and (c) correspondent positions from the casting bottom from where the specimens for tensile tests were extracted.

for each selected position. The yield (0.2% proof stress) and ultimate tensile strengths have been determined at different positions along the casting length.

3.3. Corrosion tests

As similarly conducted in previous experimental investigations [26–34], both a potentiodynamic polarization method and a qualitative electrochemical technique were chosen in order to provide consistent and useful ways to investigate the tendency of the corrosion resistance.

Electrochemical corrosion tests were performed in a 1 cm^2 circular area of ground (600 grit SiC finish) alloy samples. Electrochemical impedance spectroscopy (EIS) measurements began after an initial delay of 30 min for the samples to reach a steady-state condition. The tests were carried out with the samples immersed in a stagnant and naturally aerated 500 cm^3 of a 0.5 M H_2SO_4 solution at 25 °C under a pH of about 0.90 (±0.04), used to simulate the battery electrolytic fluid. A potentiostat (EG & G Princeton Applied Research, model 273A) coupled to a frequency analyzer system (Solartron model 1250), a glass corrosion cell kit with a platinum counter-electrode and a saturated calomel reference electrode (SCE) were used to perform the EIS tests. The potential amplitude was set to 10 mV at open-circuit, peak-to-peak (AC signal), with 5 points per decade and the frequency range was set from 100 mHz to 100 kHz. The samples were further ground to a 1200 grit SiC finish, followed by distilled water washing and air drying before measurements.

Potentiodynamic measurements were also carried out in the aforementioned solution at 25 °C using a potentiostat at the same positions where the EIS tests were carried out. These tests were conducted by stepping the potential at a scan rate of 0.2 mV s^{-1} from −0.800 mV (SCE) to +2800 mV (SCE) at open-circuit. Using an automatic data acquisition system, the potentiodynamic polarization curves were plotted and both corrosion rate and potential were estimated by Tafel plots by using both anodic and cathodic branches at a scan rate of 0.2 mV s^{-1} from −250 mV (SCE) to +250 mV (SCE) at open-circuit. This mentioned potentiodynamic range corresponds to −1200 and −700 mV vs. Hg/Hg_2SO_4 electrode (MSE). Duplicate tests for EIS and potentiodynamic polarization curves were carried out. In order to supply quantitative support for discussions of these experimental EIS results, an appropriate model (ZView version 2.1b) for equivalent circuit quantification has also been used.

4. Results and discussion

4.1. Solidification thermal variables

The temperature files containing the experimentally monitored temperatures were coupled to a finite difference solidification model [35] for determining the transient metal/mold heat transfer coefficient (h_i). The method, which is based on the solution of the inverse heat conduction problem, has been used in recent articles to determine h_i for a number of solidification situations [35,36]. Fig. 2 shows the typical experimental thermal responses (at different positions from the bottom of the casting: 4, 12, 22 and 38 mm) compared to those numerically simulated and the resulting expression relating h_i (W m^{-2} K^{-1}) to time (s) for both Pb–1 wt% Sn and Pb–2.5 wt% Sn alloys. The results of experimental thermal analysis inside the casting have also been used to determine the tip cooling rate ($\dot{T}_L$), as a function of position. The cooling rate was computed by determining the slope of the experimental cooling curves immediately after the passing of the liquidus front by each thermocouple inside the casting.

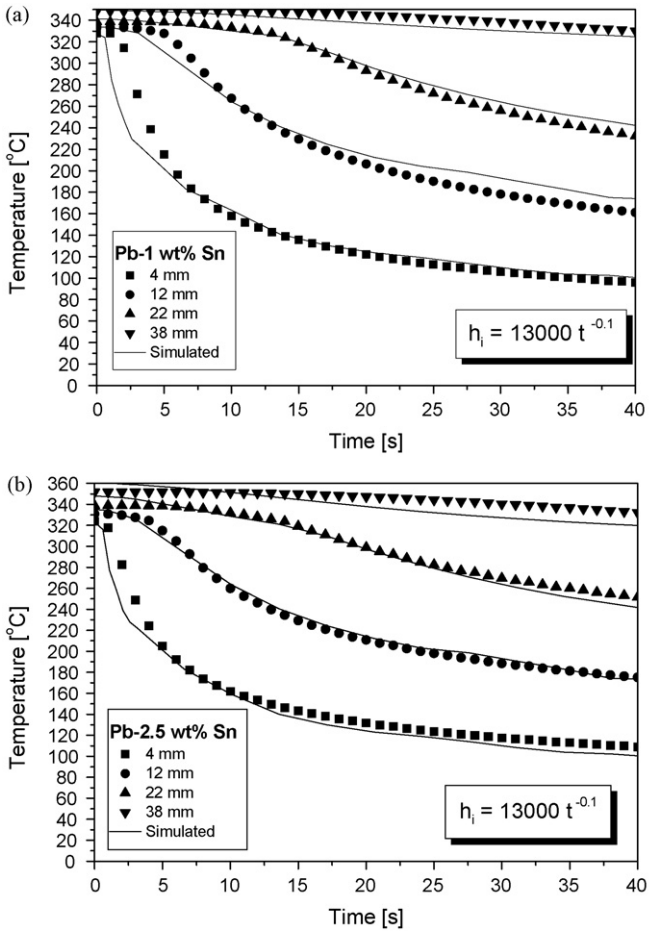

Fig. 2. Typical experimental thermal responses compared to numerical simulations for: (a) Pb–1 wt% Sn and (b) Pb–2.5 wt% Sn alloys as a function of time [s].

Fig. 3 shows a comparison between the experimental and simulated [36,37] tip cooling rate as a function of position from the metal/mold interface. Eventual discrepancies between experimental and calculated tip cooling rate are mainly caused by uncertainties in the thermophysical properties (Table 1). It can be observed that both the resulting h_i profiles as a function of time and the tip cooling rate as a function of position

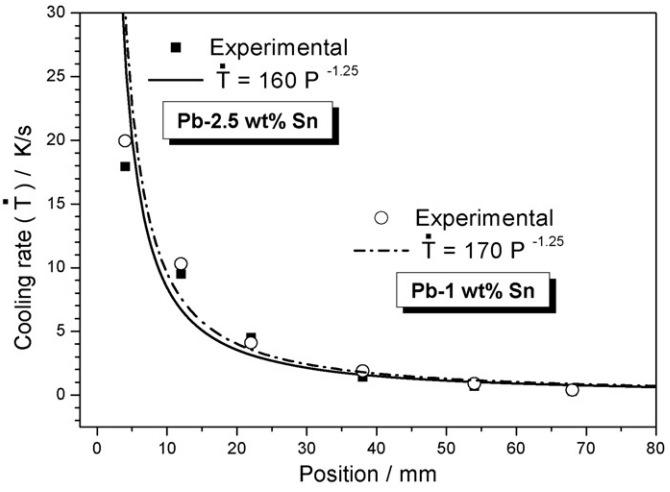

Fig. 3. Experimental and simulated tip cooling rate ($\dot{T}$) as a function of position from the bottom of the casting for Pb–1 wt% Sn and Pb–2.5 wt% Sn alloys.

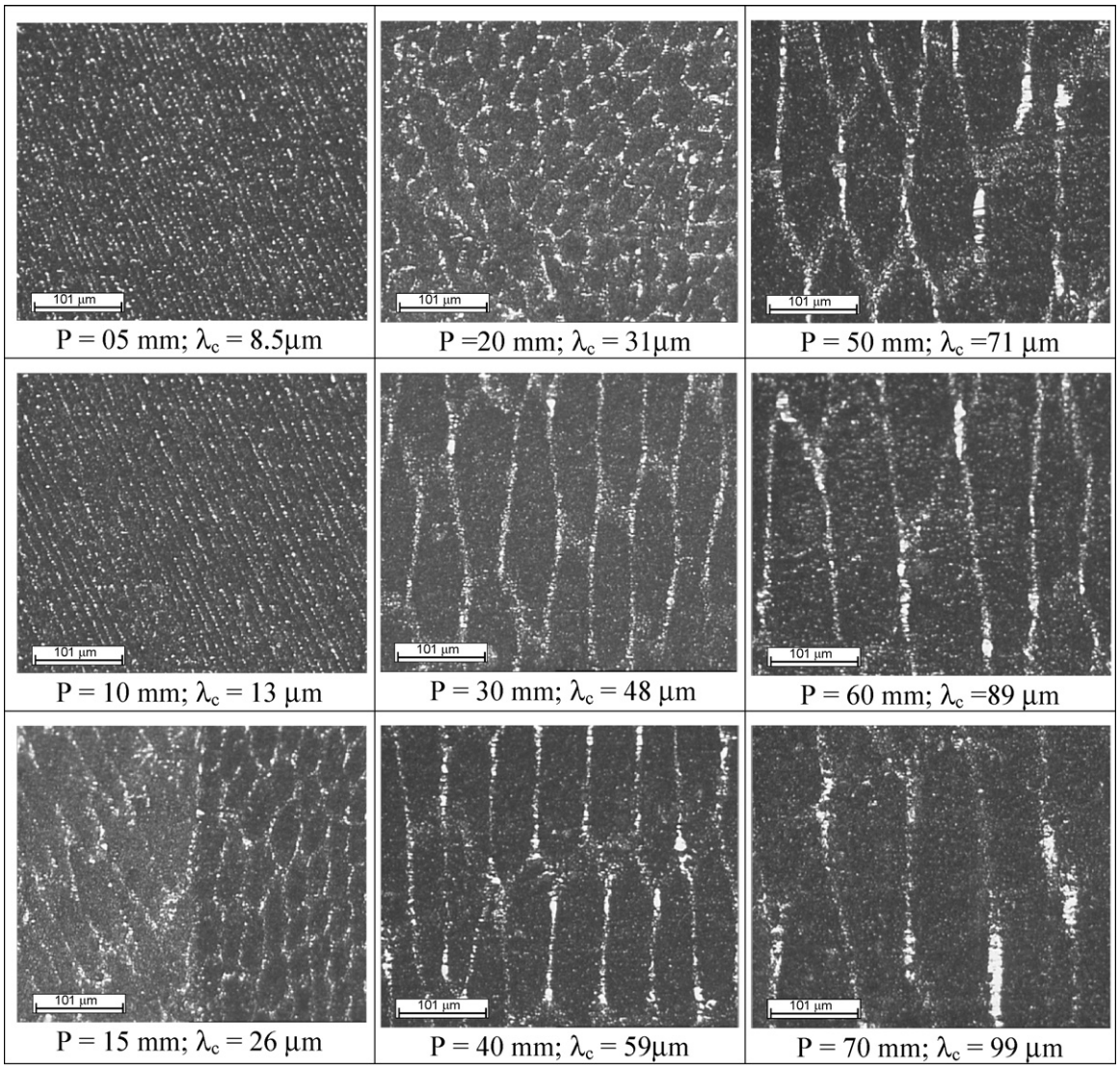

Fig. 4. Typical microstructures observed along at longitudinal sections and at different locations (5, 10, 15, 20, 30 40, 50, 60 and 70 mm) from the bottom of the casting for the Pb–1 wt% Sn alloy (optical magnification: 125×).

from the bottom of the casting are similar for the two alloys examined.

4.2. Microstructures

Typical microstructures observed at longitudinal sections along the castings length of Pb–1 wt% Sn and Pb–2.5 wt% Sn alloys are shown in Figs. 4 and 5, respectively. The as-cast microstructures have a morphology which is exclusively cellular and constituted by a Pb-rich matrix (α-phase: solid solution of Sn in Pb) with a possible eutectic mixture in the intercellular regions. The Pb-rich cellular matrix is depicted by dark regions with the intercellular eutectic mixture being represented by light regions. A water-cooled mold imposes higher values of cooling rates near the casting/cooled surface (bottom) and a decreasing profile along the casting length (top) due to the increase in thermal resistance of the solidified shell with distance from the cooled surface, as reported in previous articles [30–34]. This influence translates to the cellular growth, with smaller cell spacings near the bottom and larger ones close to the top of the casting, as shown by the microstructures of Figs. 4 and 5.

Fig. 6 shows the cellular spacing (λ_c) as a function of cooling rate ($\dot{T}$) for both Pb–1 wt% Sn and Pb–2.5 wt% Sn alloys. It can be observed that, as expected, λ_c increases due to the decrease in cooling rate with increasing distance from the bottom of the casting. The cell spacing variation with cooling rate is characterized by −0.55 power laws. This same exponent was reported by Rocha et al. [38], Rosa et al. [39] and Goulart et al. [40] concerning the cellular growth of dilute Sn–Pb, Pb–Sb and Al–Fe alloys directionally solidified under unsteady-state conditions.

4.3. Cellular array and mechanical properties

Fig. 7(a) and (b) shows typical stress–strain curves of Pb–1 wt% Sn and Pb–2.5 wt% Sn alloys for specimens extracted from different positions along the casting length, as shown in Fig. 1(c). It can be seen that in both cases the mechanical strength decreases from the bottom to the top of the casting, due to the corresponding variations in microstructure, mainly in the scale of the cellular spacing.

Fig. 8 depicts the experimental results of ultimate tensile strength (σ_U) and yield strength ($\sigma_{y=0.2}$) as a function of cellular spacing (λ_c), for the Pb–1 and Pb–2.5 wt% Sn alloys. It can be seen for both alloys σ_U increases with decreasing cellular spacing. The segregated solute (tin) will lead to the formation of eutectic mixture in the intercellular region, which together with the cell boundary

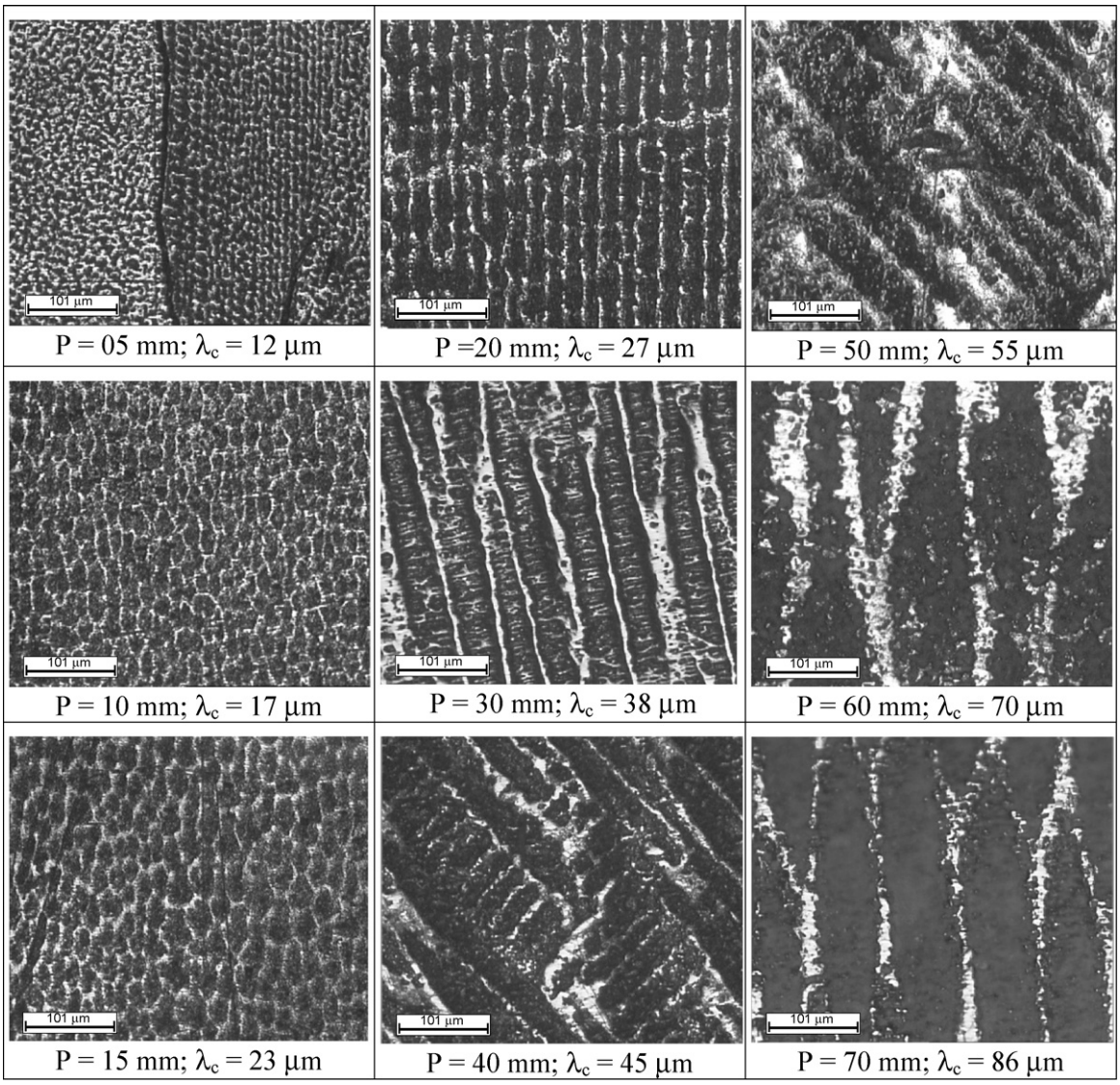

Fig. 5. Typical microstructures observed along at longitudinal sections and at different locations (5, 10, 15, 20, 30 40, 50, 60 and 70 mm) from the bottom of the casting for the Pb–2.5 wt% Sn alloy (optical magnification: 125×).

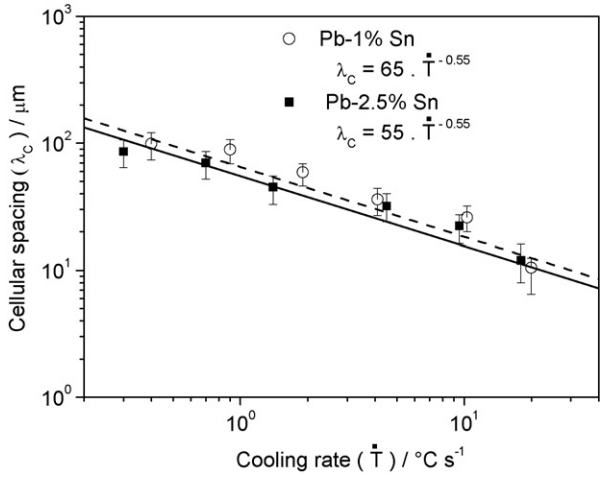

Fig. 6. Experimental cellular spacing (λ_c) vs. tip cooling rate ($\dot{T}$) for Pb–1 wt% Sn and Pb–2.5 wt% Sn alloys.

will constitute effective barriers to slip. The eutectic fraction in the intercellular region increases as the alloy Sn content is increased. The improvement in strength by reducing λ_c seems to be the result of a number of separate effects, all of which seem to operate beneficially [23–26]. As λ_c is reduced, the as-cast structure becomes cleaner and sounder and these qualities are important contributors to improved properties [23–26,41]. The increase in cooling rate has other general beneficial attributes besides the refined microstructure, e.g., the reduction in gas porosity and greater solute saturation [26]. Therefore the observed improvement in tensile properties cannot be attributed solely to the cellular arrangement.

The yield strength was shown to be essentially constant with increasing cellular spacing for the Pb–1 wt% Sn alloy, but increases slithgly with decreasing λ_c for the Pb–2.5 wt% Sn alloy. A similar observation concerning Al–Si alloys has also been reported [42,26]. It should be emphasized that the 0.2% proof stress does not strictly represent the limit between elastic and plastic tensile properties. The cellular arrangement is not expected to affect significantly the elastic deformation, but it will affect the plastic deformation so that the influence will depend on how deep in the plastic region the

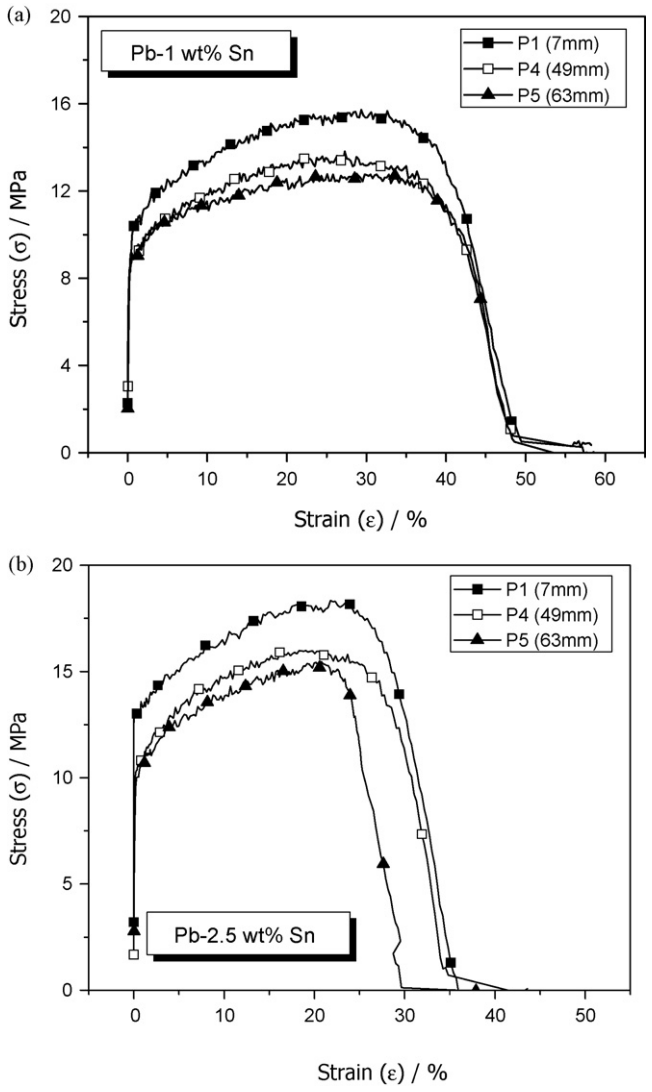

Fig. 7. Typical stress–strain curves as a function of specific positions of: (a) Pb–1 wt% Sn and (b) Pb–2.5 wt% Sn alloys.

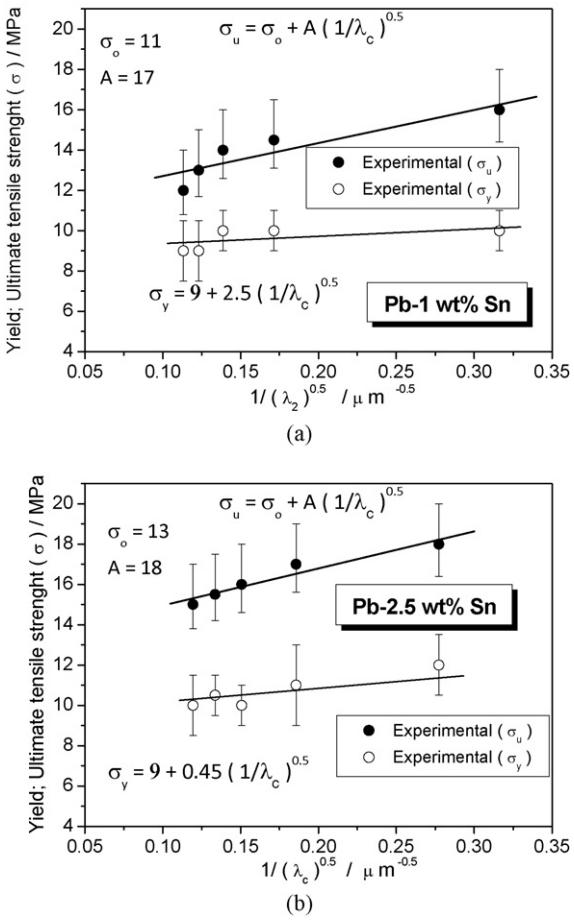

Fig. 8. Typical stress–strain curves as a function of cellular spacing: (a) Pb–1 wt% Sn and (b) Pb–2.5 wt% Sn alloys.

proof stress will be located and on the particular progress of plastic deformation of each Pb–Sn alloy.

As previously reported [23–26], the experimental equations appearing in Fig. 8 can incorporate models expressing λ_c as a function of thermal solidification variables permitting expressions correlating mechanical properties with solidification conditions to be established.

4.4. Cellular array and electrochemical behavior

In order to investigate the corrosion resistance of dilute Pb–Sn alloys as a function of cell spacing, samples extracted from three different positions along the casting length (two samples for each position) were subjected to corrosion tests (EIS and Tafel polarization techniques). An equivalent circuit has been proposed and the interpretation of the physical elements in the circuit has also been used in order to fit the experimental data, as reported in previous articles [31–34].

Fig. 9 shows simulated and experimental corrosion results in Nyquist diagrams corresponding to tests carried out with Pb–1 wt% Sn and Pb–2.5 wt% Sn alloy samples in a 0.5 M sulfuric acid solution at room temperature. The corresponding microstructures corresponding to each position from where the samples were extracted along the casting length are also shown in Fig. 9. All complex plane plots (Nyquist plots) are characterized by a capacitive arc at high frequencies (between 10^5 and 1 Hz) followed by a slope of about 45° at frequencies lower than 1 Hz [34]. These Nyquist plots reveal that the diameters of the capacitive arcs for coarser cellular spacing (position P3) are higher than those for finer cellular spacing (positions P2 and P1) for both Pb–1 wt% Sn and Pb–2.5 wt% Sn alloys. In previous articles [33,34] both Bode and Bode-phase diagrams and potentiodynamic polarization curves which resulted from these corrosion tests have been extensively discussed. It was concluded that a coarser cellular array has better electrochemical behavior than a finer cellular array. These parameters evidence that coarser cells tend to improve the corrosion resistance of both Pb–1 wt% Sn and Pb–2.5 wt% Sn alloys mainly due to the reduction of cellular boundaries. Table 2 summarizes the current densities and

Table 2
Experimental current density and corrosion potential for the Pb–1 wt% Sn and Pb–2.5 wt% Sn alloys.

Alloy	Position	Current density (i) ($\mu A\,cm^{-2}$)	Corrosion potential [E] (mV)
Pb–1.0 wt% Sn	P1	46 (±5)	−538
	P2	24 (±3)	−535
	P3	8.5 (±5)	−528
Pb–2.5 wt% Sn	P1	58 (±6)	−543
	P2	38 (±4)	−540
	P3	19 (±2)	−537

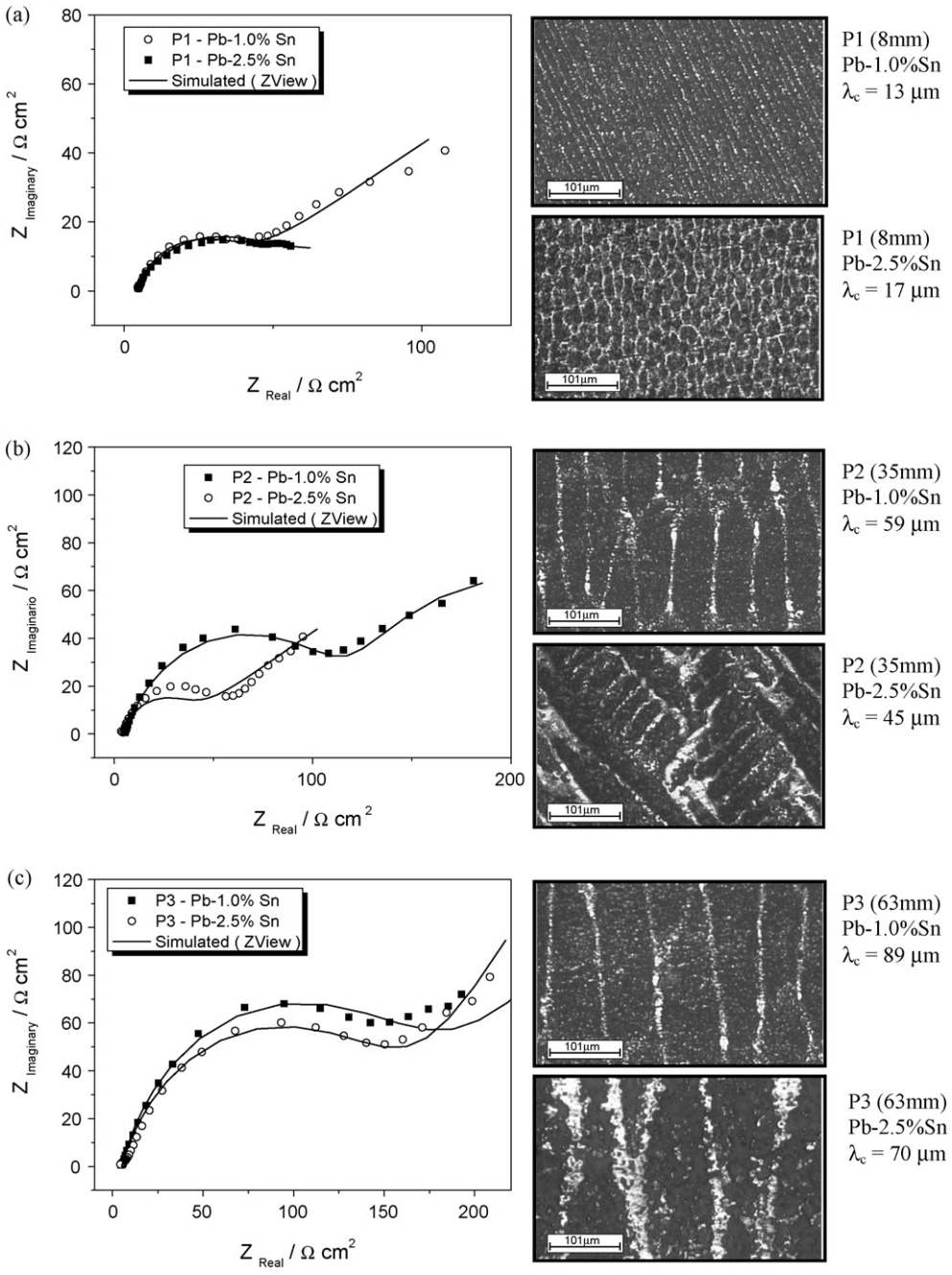

Fig. 9. Comparison between simulated and experimental Nyquist plots and corresponding microstructures for each position for Pb–1% Sn and Pb–2.5% Sn alloys in: (a) P1, (b) P2 and (c) P3.

corrosion potentials for the Pb–1 wt% Sn and Pb–2.5 wt% Sn alloys [34].

Although Simon et al. [43] reported that the Pb–1 wt% Sn alloy has better corrosion resistance than the Pb–2.5 wt% Sn alloy, in the present experimental study, a similar tendency in terms of electrochemical corrosion response as a function of cellular array has been observed. Xu et al. [44] concluded that Pb–Sn alloys have the best corrosion resistance for Sn concentrations between 2 and 3 wt%. They reported that a Pb–2.6 wt% Sn alloy was found to have a higher electrochemical corrosion resistance than a Pb–1 wt% Sn alloy. However, their experimental results were not provided as a function of the resulting microstructure. Xu et al. [44] have also reported the occurrence of passive layers and pitting formation.

4.5. Correlation between corrosion resistance and mechanical properties

Fig. 10 summarizes the experimental corrosion resistance and ultimate tensile strength (UTS) plotted as a function of cellular spacing for both Pb–1 wt% Sn and Pb–2.5 wt% Sn alloys. In order to compare the behavior of corrosion resistance and tensile strength, the corrosion resistance (CR) is represented by the inverse of the current density and the UTS values are those indicated in Fig. 8.

It is well known that the great challenge in engineering applications is the improvement of a property without provoking deleterious effects in another property. Thus, the aim of such combined plots is to design an “ideal” range of microstructural cellular spacings permitting a compromise between good corrosion resis-

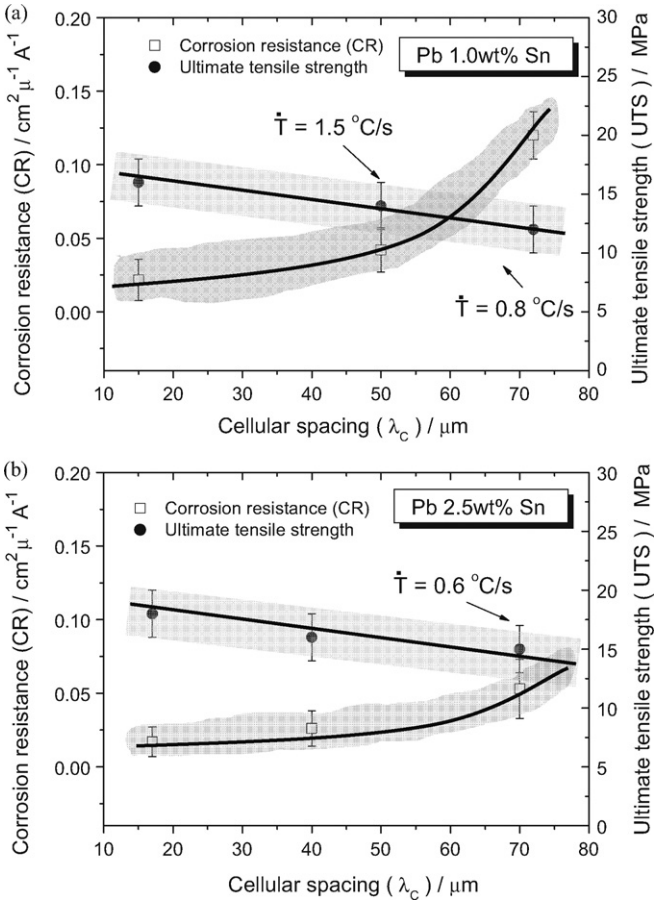

Fig. 10. Correlation between experimental corrosion resistance (CR), ultimate tensile strength (UTS) and cellular spacings (λ_c) associated with cooling rate ($\dot{T}$) for: (a) Pb–1%wt Sn and (b) Pb–2.5 wt% Sn alloys.

tance (CR) and good tensile strength (UTS) to be established for these alloys. Evidently, for some specific application where one of these characteristics should be more significant than the other one, this range of equilibrium between CR and UTS should not be considered. It can also be observed that an "ideal" range combining CR and UTS for the Pb–1 wt% Sn alloy lies between 50 and 65 μm, which can be associated with cooling rates during casting from 1.5 to 0.8 °C s^{-1}. On the other hand, the Pb–2.5 wt% Sn alloy depicts a slightly higher range, i.e., cell spacings between 70 and 75 μm corresponding to cooling rates between 0.6 and 0.5 °C s^{-1}, as shown in Fig. 10.

The manufacturers are continuously searching for modifications in the grid manufacturing processes [1–7] with a view to decrease battery grid weight as well as to reduce the production costs for applications in automotive and telecommunication fields as VRLA or SLI batteries [1–4]. As the electrochemical corrosion behavior of the Pb–1 wt% Sn and Pb–2.5 wt% Sn alloys are very similar, when a same order of magnitude of the cellular array is considered, the production of battery components using the Pb–2.5 wt% Sn alloy can considerably decrease the final battery weight. In a previous article, it was shown that the use of a Pb–2.5 wt% Sn alloy for manufacturing battery grids may induce a single battery unit to be from 200 to 300 g lighter than a similar one manufactured with a Pb–1 wt% Sn alloy [34].

5. Conclusions

The following major conclusions can be drawn from the present experimental study:

- The cell spacing variation with cooling rate during casting has been characterized by −0.55 power laws given by: $\lambda_c = 65\ \dot{T}^{-0.55}$ and $\lambda_c = 55\ \dot{T}^{-0.55}$, λ_c [μm] and $\dot{T}$ [°C s^{-1}], for the Pb–1 wt% Sn and Pb–2.5 wt% Sn alloys, respectively.
- The ultimate tensile strength increases with decreasing cellular spacing for both the Pb–1 wt% Sn and Pb–2.5 wt% Sn alloys. The yield strength was shown to be essentially constant with increasing cellular spacing for the Pb–1 wt% Sn alloy, but increases slithgly with decreasing λ_c for the Pb–2.5 wt% Sn alloy.
- Coarser cells tend to improve the corrosion resistance of both Pb–1 wt% Sn and Pb–2.5 wt% Sn alloys mainly due to the reduction of cellular boundaries.
- A combined plot of corrosion resistance and ultimate tensile strength as a function of cellular spacing has permitted a compromise between both good corrosion resistance and good mechanical properties to be attained by choosing appropriate cell spacing ranges for each alloy. These ranges were shown to be associated with cooling rates during casting from 1.5 to 0.8 °C s^{-1} and between 0.6 and 0.5 °C s^{-1} for the Pb–1 wt% Sn and Pb–2.5 wt% Sn alloys, respectively.

Acknowledgements

The authors acknowledge financial support provided by FAPESP (The Scientific Research Foundation of the State of São Paulo, Brazil), FAEPEX-UNICAMP, and CNPq (The Brazilian Research Council).

References

[1] M.D. Achtermann, M.E. Greenlee, J. Power Sources 33 (1991) 87–92.
[2] J. Wirtz, Batteries International, 1996, p. 56.
[3] R.D. Prengaman, J. Power Sources 95 (2001) 224–233.
[4] R.D. Prengaman, Advances in lead-acid batteries, in: K.R. Bullock, D. Pavlov (Eds.), Proceedings, vol. 84–14, The Electrochemical Society Pennington, NJ, 1984, p. 201.
[5] R.D. Prengaman, J. Power Sources 158 (2006) 1110–1116.
[6] G.S. Al-Ganainy, M.T. Mostafa, F. Abd El-Salam, Physica B 348 (2004) 242–248.
[7] B. Rezaei, S. Damiri, J. Solid State Electrochem. 9 (2005) 590–594.
[8] M. Shiota, T. Kameda, K. Matsui, N. Hirai, T. Tanaka, J. Power Sources 144 (2005) 358–364.
[9] T. Hirasawa, K. Sasaki, M. Taguchi, H. Kaneko, J. Power Sources 85 (2000) 44–48.
[10] C.S. Lakshmi, J.E. Manders, D.M. Rice, J. Power Sources 73 (1998) 23–29.
[11] S. Stein, G. Bourguinon, L. Raboin, L. Broch, L. Johann, E. Rocca, Thin Solid Films 455–456 (2004) 735–741.
[12] D. Slavkov, B.S. Haran, B.N. Popov, F. Fleming, J. Power Sources 112 (2002) 199–208.
[13] L.T. Lam, N.P. Haigh, D.A.J. Rand, J. Power Sources 88 (2000) 11–17.
[14] E. Hilali, L. Bouirden, Ann. Chim. Sci. Mater. 25 (2000) 91–100.
[15] H.-Y. Chen, S. Li, D. Shu, W.S. Li, C.L. Dou, Q. Wang, J. Power Sources 168 (2007) 79–89.
[16] A. Li, Y. Cheni, H. Chen, D. Shu, W. Li, H. Wang, C. Dou, W. Zhang, S. Chen, J. Power Sources 189 (2009) 1204–1211.
[17] W.X. Guo, D. Shu, H.Y. Chen, A.J. Li, H. Wang, G.M. Xiao, C.L. Dou, S.G. Peng, W.W. Wei, W. Zhang, H.W. Zhou, S. Chen, J. Alloys Compd. 475 (2009) 102–109.
[18] N.J. Petch, J. Iron Steel Inst. 174 (1953) 25–31.
[19] A. Lasalmonie, J. Strudel, J. Mater. Sci. 21 (1986) 1837–1852.
[20] K.J. Kurzydlowski, B. Ralph, J.J. Bucki, A. Garbacz, Mater. Sci. Eng. A 205 (1996) 127–132.
[21] D. Dubé, A. Couture, Y. Carbonneaut, M. Fiset, R. Angers, R. Tremblay, Int. J. Cast Met. Res. 11 (1998) 139–144.
[22] P. Donelan, Mater. Sci. Technol. 16 (2000) 261–269.
[23] W.R. Osório, A. Garcia, Mater. Sci. Eng. A 325 (2002) 103–111.
[24] W.R. Osório, C.A. Santos, J.M.V. Quaresma, A. Garcia, J. Mater. Proc. Technol. 143 (2003) 703–709.
[25] J.M. Quaresma, C.A. Santos, A. Garcia, Metall. Mater. Trans. A 31 (2000) 3167–3178.
[26] W.R. Osório, P.R. Goulart, G.A. Santos, C. Moura Neto, A. Garcia, Metall. Mater. Trans. A 37 (2006) 2525–2537.
[27] W.R. Osório, C.M.A. Freire, A. Garcia, J. Alloys Compd. 397 (2005) 179–191.
[28] W.R. Osório, J.E. Spinelli, N. Cheung, A. Garcia, Mater. Sci. Eng. A 420 (2006) 179–186.
[29] W.R. Osório, C.M.A. Freire, A. Garcia, J. Mater. Sci. 40 (2005) 4493–4499.
[30] W.R. Osório, D.M. Rosa, A. Garcia, J. Power Sources 175 (2008) 595–603.
[31] D.M. Rosa, J.E. Spinelli, W.R. Osório, A. Garcia, J Power Sources 162 (2006) 696–705.
[32] W.R. Osório, C. Aoki, A. Garcia, J. Power Sources 185 (2008) 1471–1477.
[33] L.C. Peixoto, W.R. Osório, A. Garcia, J. Power Sources 192 (2009) 724–729.

[34] W.R. Osório, L.C. Peixoto, A. Garcia, J. Power Sources 194 (2009) 1120–1127.
[35] N. Cheung, N.S. Santos, J.M.V. Quaresma, G.S. Dulikravich, A. Garcia, Int. J. Heat Mass Transfer 52 (2009) 451–459.
[36] N. Cheung, I.L. Ferreira, M.M. Pariona, J.M.V. Quaresma, A. Garcia, Mater. Des. 30 (2009) 3592–3601.
[37] F. Sá, O.L. Rocha, C.A. Siqueira, A. Garcia, Mater. Sci. Eng. A 373 (2004) 131–138.
[38] O.L. Rocha, C.A. Siqueira, A. Garcia, Mater. Sci. Eng. A 361 (2003) 111–118.
[39] D.M. Rosa, J.E. Spinelli, I.L. Ferreira, A. Garcia, J. Alloys Compd. 422 (2006) 227–238.
[40] P.R. Goulart, K.S. Cruz, J.E. Spinelli, I.L. Ferreira, N. Cheung, A. Garcia, J. Alloys Compd. 470 (2009) 589–599.
[41] J. Campbell, Castings, Butterworth–Heinemann, Oxford, United Kingdom, 1991, pp. 264–267.
[42] E.L. Rooy, Aluminum and aluminum alloys in castings, in: Metals Handbook, vol. 15, ASM International, Metals Park, Ohio, USA, 1988, pp. 743–770.
[43] P. Simon, N. Bui, N. Pebere, F. Dabosi, L. Albert, J. Power Sources 55 (1995) 63–71.
[44] J. Xu, X. Liu, X. Li, E. Barbero, C. Dong, J. Power Sources 155 (2006) 420–427.